

A possible transit of a disintegrating exoplanet in the nearby multiplanet system DMPP-1

MARK H. JONES,¹ CAROLE A. HASWELL,¹ JOHN R. BARNES,¹ DANIEL STAAB,^{1,*} AND RENÉ HELLER²

¹*School of Physical Sciences, The Open University, Milton Keynes, MK7 6AA, U.K.*

²*Max Planck Institute for Solar System Research, Justus-von-Liebig-Weg 3, 37077 Göttingen, Germany*

(Received 2020 March 17; Revised 2020 April 30; Accepted 2020 May 1)

Submitted to ApJL

ABSTRACT

We analyse TESS photometry of DMPP-1 (HD 38677; TIC 66560666), a nearby F8V star hosting hot super-Earth planets and a warm Neptune. Using the Transit Least Squares algorithm and other methods we find a transit signal at $P = 3.2854_{-0.0025}^{+0.0032}$ d with depth 87_{-30}^{+25} ppm and false alarm probability 1.6%. This is shallower than hitherto published TESS discoveries. The 3.285 d signal is recovered for several, but not all, methods for detrending stellar astrophysical variability. Further observations are needed to improve the significance of the detection. If this transit were due to an Earth-like rocky planet it would have been detected in the RV data, but it is not. The TESS data cover seven individual transits, one of which is consistent with zero depth. The insolation of the putative planet is $990S_{\oplus}$, typical of fluxes experienced by the three known catastrophically disintegrating exoplanets (CDEs). The transits can be self-consistently attributed to a CDE with a mass below the RV detection threshold. We searched for transits of the known RV planets, finding null results and detection thresholds of < 100 ppm, which we quantify for each. The DMPP-1 planetary system was discovered as a consequence of circumstellar gas attributed to ablation of hot planets. The RV planets may have been ablated to near-pure iron cores. We place limits on the orbital inclinations of the RV planets where the expected transit depth exceeds the detection threshold. If the 3.2854 day transit detection is confirmed, e.g. with CHEOPS photometry, DMPP-1 would be a first-rate target for JWST spectroscopy.

1. INTRODUCTION

Terrestrial exoplanet research began with the discovery of CoRoT-7 b (Léger et al. 2009). Since then Kepler has shown that small, presumably rocky planets are common in orbits smaller than that of Mercury. Among Kepler’s most exciting rocky planet discoveries are the catastrophically disintegrating exoplanets (CDEs), with prototype Kepler-1520 b (Rappaport et al. 2012). These hot, low mass, rocky planets are heated to temperatures ~ 2000 K at the substellar point so that the rocky surface sublimates. Dust condenses from the metal-rich vapour producing variable-depth transits of the dust clouds orbiting with the undetectably small ablating planets.

Kepler-1520 is a $V = 16$ K star; brighter, nearby analogues and progenitors would allow exciting opportunities to probe the mineral composition of rocky planets outside our own Solar System (Bodman et al. 2018). TESS (Ricker et al. 2015) is performing an (almost) all sky transit survey and should find such objects.

The Dispersed Matter Planet Project (DMPP, Haswell et al. 2019) is an RV planet search which was partly motivated by the goal of detecting nearby CDEs and their progenitors. WASP-12 and other host stars of close-orbiting planets are shrouded in gas which absorbs the stellar chromospheric emission (Haswell et al. 2012; Fossati et al. 2013; Staab et al. 2017). Thus anomalously low chromospheric emission can indicate hot, mass-losing planets. DMPP uses the widely-adopted metric of stellar activity, $\log R'_{\text{HK}}$, which is derived from the Mount Wilson S-index (Noyes et al. 1984), to select bright FGK V stars with apparently anomalously low chromospheric emission. This is attributed to absorption by metal-rich circumstellar gas ablated from hitherto undiscovered hot planets. Because these are the easiest stars for

Corresponding author: M.H.Jones
m.h.jones@open.ac.uk

* AVS, Rutherford Appleton Laboratory, Harwell, Oxford, U.K.

RV planet discoveries, the hypothesis underlying DMPP was that many of the targets will host ablating low mass, presumably rocky, planets. CDEs constitute the most dramatic examples of such planets. DMPP-1 (HD 38677) is a nearby bright analogue of the Kepler compact multiplanet systems (Staab et al. 2019) orbiting a F8V host star with $V = 7.98$. The system contains at least three super-Earth planets ($M_P \sin i$ values of 1.8–9.6 M_\oplus) interior to a Neptune-like planet on a 19 d orbit. Gas ablated from an orbiting planet will be concentrated in the orbital plane, so DMPP should preferentially pick out ablating planet systems with an edge-on orientation. Thus we expect higher than random transit probabilities for the DMPP systems. This paper reports an analysis of the TESS light curve for DMPP-1.

In Section 2 we describe the TESS data and the removal of systematic instrumental and astrophysical trends; the details of the approach affect the results of the transit searches we describe in Section 3. Section 4 discusses our findings and their broader implications. Finally, Section 5 briefly summarises our conclusions.

2. DATA AND METHODS

TESS continuously covers 2304 square degrees (a Sector) for ~ 27 days obtaining photometry in the 600–1000 nm bandpass at 2 minute cadence on selected targets. DMPP-1 was observed with TESS Camera 2, CCD 4 during Sector 6 (December 2018); i.e., BTJD 1468.27 to 1490.04 (Barycentric Julian Date–2457000.0) with a ~ 1.1 d data gap at BTJD 1477.03. Pipeline processing produces a background-subtracted calibrated standard aperture photometry (SAP) light curve (Figure 1a). Subsequent removal of systematic instrumental effects yields the Pre-search Data Conditioning (PDC) flux (Figure 1b; Tenenbaum & Jenkins 2018; Smith et al. 2017) with a mean value of $1.5995 \times 10^5 \text{ e s}^{-1}$. The smooth residual modulation on a time-scale of several days is assumed to be astrophysical.

Before our transit searches we: (i) rejected data with quality flag values < 512 (Tenenbaum & Jenkins 2018, Table 28) leaving 14827 cadences; (ii) recursively removed outliers exceeding the median flux (of the entire light curve) by more than three standard deviations (‘sigma-clipping’), rejecting 69 data points (c.f. 20 points if the data were Gaussian distributed); (iii) detrended this cleaned light curve using Gaussian Processes (GP) as described below. Sigma-clipping was implemented using `lightkurve` (Lightkurve Collaboration 2018).

We modelled the smooth modulation with `Celerite` (Foreman-Mackey et al. 2017). A GP kernel comprising a single damped harmonic oscillator with damping parameter $Q = 1/\sqrt{2}$ is sufficient to model the smooth variability, finding a characteristic frequency $\omega_0 = 1.48 \text{ rad day}^{-1}$.

Dividing by the mean GP function (red trace in Figure 1c) yields the detrended, normalised light curve shown in Figure 1d and used for subsequent analyses. GP detrending reduced the standard deviation of the sigma-clipped PDC light curve from 302 ppm to 293 ppm.

3. TRANSIT SEARCHES

The RV measurements of DMPP-1 were used to derive a preferred solution of four planets (see Table 1a), and an alternative, less probable solution in which the data are modelled with an S-index correlation term (Staab et al. 2019, Table 1b). For completeness both solutions are considered here. The light curve spans 21.8 d, so we searched for repeated transits at $P < 10.9$ d and for single and partial transits due to longer period planets. For clarity, we denote *expected* transit depths by δ and *measured* flux changes (or limits) by $(\Delta F/F)$ (with measurement time-scale).

3.1. Signal limits at given periods

The Keplerian RV modulations of DMPP-1 c, d, e, d', e' and f' (Table 1) have $P < 10.9$ d, so we folded the light curve to search for modulation using a range of phase binning. The maximum bin width used was $(T_{\text{dur, max}}/P) = R_*/(\pi a)$, where $T_{\text{dur, max}}$ is the maximum transit duration (i.e. for inclination $i = 90^\circ$) of a planet in a circular orbit, a is the semi-major axis, and R_* is the stellar radius. The minimum bin width was 0.05 of the maximum value, and ranges from 8.48 minutes (DMPP-1 f') to 12.07 minutes (DMPP-1 c). Every binning searched 10 starting ephemerides spread uniformly over a bin width. The significance of any decrease in normalised flux from the mean value of 1.00 is expressed in terms of the standard error of the mean (derived from individual measurement uncertainties) in the corresponding phase bin (σ_{bin}). For every folding, the most significant decrease (‘dip’) was identified.

We found no signal with a significance exceeding $5\sigma_{\text{bin}}$. The $5\sigma_{\text{bin}}$ upper limits (at a given bin width) are shown as solid black lines in Figure 2a–f, with the limit at maximum bin size $(\Delta F/F)_{\text{max}}$ listed in Table 1.

To assess expected transit signals we created synthetic light curves using the `batman` package (Kreidberg 2015), analysing them as above. Planetary radii, $R_{P, \text{Earth-like}}$, are estimated from the minimum masses $M_P \sin i$ given by

(a) Preferred solution					
	DMPP-1 b	DMPP-1 c	DMPP-1 d	DMPP-1 e	
P [d]	18.57	6.584	2.882	5.516	
a [AU]	0.1462	0.0733	0.0422	0.0651	
$M_P \sin i$ [M_\oplus]	24.27	9.60	3.35	4.13	
S [S_\oplus]	98	390	1177	494	
$R_{P, \text{Earth-like}}$ [R_\oplus]		1.814	1.393	1.471	
$R_{P, \text{Fe}}$ [R_\oplus]		1.434	1.126	1.184	
$R_{P, \text{H}_2\text{O}}$ [R_\oplus]	3.243				
δ_0 [ppm]	649	203 [†] , 127 [‡]	120 [†] , 78 [‡]	134 [†] , 87 [‡]	
Method	‘step’	‘fold’	‘fold’	‘fold’	
$T_{\text{dur, max}}$ [d]	0.237	0.168	0.127	0.158	
$(\Delta F/F)_{\text{max}}$ [ppm]	< 158	< 93	< 57	< 78	
b (Earth-like)	> 0.974 [#]	> 0.880	> 0.877	> 0.856	
b (pure iron)		> 0.591	> 0.621	—	
i (Earth-like)	< 87.76 ^{o#}	< 85.96 ^o	< 83.00 ^o	< 85.93 ^o	
i (pure iron)		< 87.26 ^o	< 85.05 ^o	—	
(b) Solution with S-index correlation					
	DMPP-1 b’	DMPP-1 c’	DMPP-1 d’	DMPP-1 e’	DMPP-1 f’
P [d]	19.61	34.74	3.144	6.454	2.281
a [AU]	0.1517	0.2220	0.0447	0.0723	0.0361
$M_P \sin i$ [M_\oplus]	19.92	20.12	3.95	4.95	1.82
$R_{P, \text{Earth-like}}$ [R_\oplus]			1.453	1.540	1.181
$R_{P, \text{Fe}}$ [R_\oplus]			1.172	1.235	0.965
$R_{P, \text{H}_2\text{O}}$ [R_\oplus]	3.120	3.215			
δ_0 [ppm]	601	603	130 [†] , 85 [‡]	146 [†] , 94 [‡]	86 [†] , 57 [‡]
Method	‘step’	‘step’	‘fold’	‘fold’	‘fold’
$T_{\text{dur, max}}$ [d]	0.241	0.292	0.131	0.167	0.118
$(\Delta F/F)_{\text{max}}$ [ppm]	< 156	< 142	< 65	< 95	< 55
b (Earth-like)	> 0.970 [#]	> 0.976 [#]	> 0.856	> 0.699	> 0.738
b (pure iron)			> 0.531	—	—
i (Earth-like)	< 87.85 ^{o#}	< 88.52 ^{o#}	< 83.55 ^o	< 86.75 ^o	< 83.11 ^o
i (pure iron)			< 86.01 ^o	—	—
(c) Marginal detection					
R_P [R_\oplus]	1.38 ^{+0.29} _{-0.32}				
P [d]	3.2854 ^{+0.0032} _{-0.0025}				
T_0 [BTJD]	1469.982 ± 0.010				
i	83.4 ^{o+1.0} _{-0.4}				
a [AU]	0.0461 ± 0.0008				
T_{dur} [d]	0.06 ^{+0.03} _{-0.01}				
b	0.90 ^{+0.04} _{-0.13}				
δ [ppm]	87 ⁺²⁵ ₋₃₀				
$M_P, \text{Earth-like}$ [M_\oplus]	3.2 ^{+3.6} _{-2.0}				

Table 1. (a), (b) DMPP-1 RV planets from [Staab et al. \(2019\)](#) with radii, R_P , using the Earth-like, pure iron (Fe) and 100 percent water at $T = 1000$ K (H_2O) models of [Zeng et al. \(2019\)](#). δ_0 is the expected transit depth when impact parameter $b = 0$ († and ‡ indicate Earth-like and pure iron models respectively). ‘fold’ and ‘step’ denote the search methods. For b and i , # indicates the 100 percent water model ($T = 1000$ K), and entries marked ‘—’ are below the detection limit. (c) The marginally detected signal and implied planetary parameters.

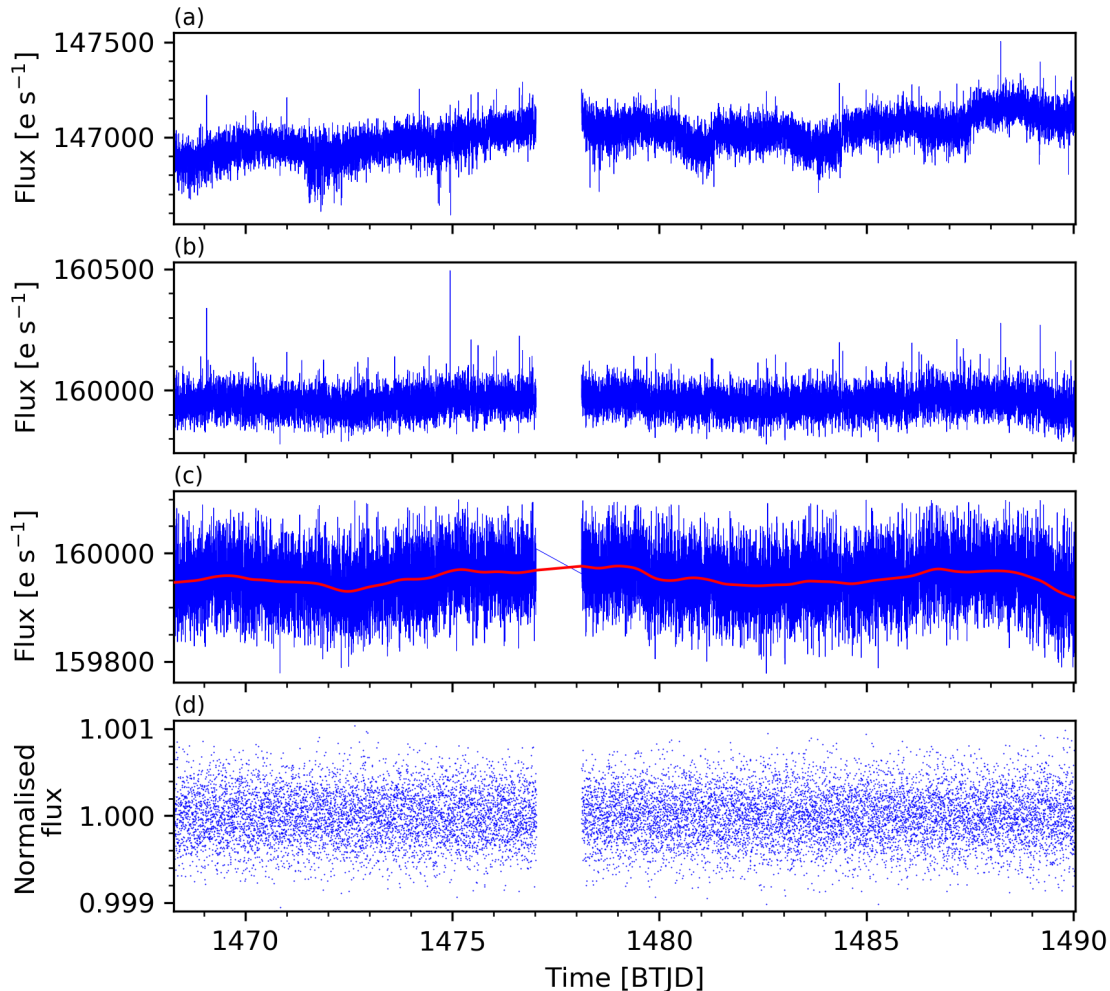


Figure 1. (a) TESS Sector 6 SAP flux of DMPP-1, (b) the corresponding PDC light curve. (c) The PDC flux light curve after sigma-clipping (blue) and the mean GP function (red). (d) The cleaned, de-trended and normalised PDC flux used for transit searches.

Staab et al. (2019), assuming $i = 90^\circ$ and the Earth-like rocky planet models of Zeng et al. (2019). Semi-major axes of (assumed circular) planetary orbits are as given by Staab et al. (2019). We adopt $R_* = 1.26R_\odot$ (Staab et al. 2019) with a quadratic limb-darkening law ($u_q = 0.3216$, $v_q = 0.2301$) appropriate for a star with $T_{\text{eff}} = 6200$ K and $\log g = 4.5$ (Stassun et al. 2018).

The responses of the search method to synthetic light curves for models with impact parameter $b = 0$ are shown (solid red lines) in Figures 2a–f noting that they approach the expected analytic transit depths δ_0 (Heller 2019, see Table 1) as bin widths become small. All signals (for $b = 0$, $i = 90^\circ$) exceed the $5\sigma_{\text{bin}}$ detection limits and are ruled out by the data.

We investigated the detectability of grazing transits by varying b . The dotted red lines in Figure 2a–f show the minimum value of b for which the response to the model lies below $5\sigma_{\text{bin}}$ at all bin widths. These limits on b (and corresponding limits on i) are reported in Table 1.

We also considered the case of planets which are predominantly iron (blue lines in Fig. 2a–f): this produces the smallest conceivable planet radii for the measured masses. As discussed by Price & Rogers (2019) iron planets may arise from collisionally-driven mantle stripping or formation from iron-enriched material, but as discussed in Section 4.2, we propose that mantle ablation is a key process in DMPP-1. We used the pure iron planet models of Zeng et al. (2019) to derive the radii corresponding to the minimum masses of these planets (see Table 1). We establish that if planets have been ablated down to iron cores, DMPP-1 c, d and d' are potentially detectable, but only over a reduced range of

impact parameters ($b < 0.591, 0.621$ and 0.531 respectively), while DMPP-1 e, e' and f' would be too small to produce detectable transits.

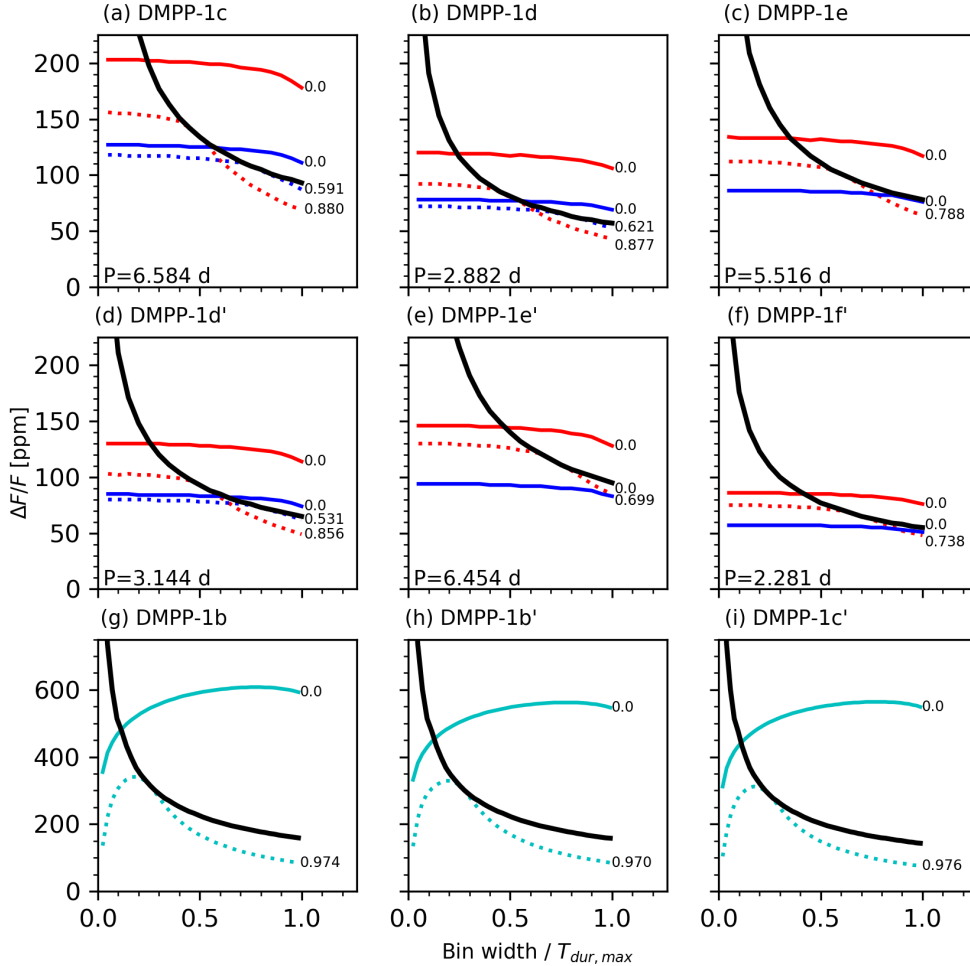


Figure 2. The 5σ limits (black line) on the amplitude of transit signals from DMPP-1 planets (Staab et al. 2019) as a function of measurement time-scale (expressed as a fraction of the maximum transit duration, $T_{dur, max} = PR_*/\pi a$). Coloured lines show the responses of the search methods with Zeng et al. (2019) density models: red – Earth-like; blue – pure iron; cyan – 100 percent water at 1000 K. Solid lines show the expected response when $b = 0$. Dotted lines show the response at the limit of detectability along with the corresponding value of b . Panels (a)–(f) are calculated using the period folding method while panels (g)–(i) are based on the step-detection method (see text for details).

3.2. Searches for Single Transits and Partial Transits

Three planets listed in Table 1 (DMPP-1 b, b' and c') have periods which produce folded TESS light curves with incomplete phase coverage due to data gaps, or which could only exhibit a single transit. However, the radii of these planets (implied by $M_P \sin i$) potentially allows single and partial transits to be detected from step-like changes in flux. Step detection was based on the difference between the mean fluxes in two equal-sized bins before and after a given time, with the significance of any change assessed in terms of the uncertainty (σ_{step}). We varied the bin width, from 4 to 216 cadences, i.e. 0.0056 to 0.30 d.

No step-like features were detected in the TESS light curve at a level exceeding $5\sigma_{\text{step}}$. The maximum value of $5\sigma_{\text{step}}$ as a function of bin width is shown in Figure 2g-i (black line), with Table 1 giving the limit to any step change in flux (at a time-scale corresponding to maximum transit duration) $(\Delta F/F)_{\text{max}}$ as $5\sigma_{\text{bin}}$.

As in Section 3.1 simulated light curves were used to determine the response to transits. Assuming the mass-radius relationship for pure water planets at $T = 1000$ K given by Zeng et al. (2019) the expected maximum ($b = 0$) transit depths are ~ 600 ppm, (solid cyan lines in Figures 2g-i), and would be detected if present. To be consistent with no detected signal, $b > 0.97$ (dotted lines in Figure 2g-i; Table 1).

Alternatively, transits from DMPP-1 b, b' or c' may have been missed because their orbital periods exceed the continuous coverage the light curve. The coverage at periods of 18.57, 19.61 and 34.74 d is 94, 94, and 60 percent respectively. Thus there is a 6 percent chance that transits in DMPP-1 b and b' have been missed due to incomplete coverage, rising to a 40 percent chance for DMPP-1 c'. Further RV measurements would improve the precision of the orbital ephemerides and constrain the timings of the inferior conjunctions during the TESS coverage so these non-detections can be definitively interpreted.

3.3. Period searching using Transit Least Squares

We find no evidence for transits at the orbital periods of DMPP-1 c, d, e, d', e', f', but further low-mass planets below the current RV detection threshold may exist. Hence, we searched for transits with $P < 10.88$ d using the Transit Least Squares (TLS) method of Hippke & Heller (2019) implemented through the TLS package. This fits a transit template (derived from *Kepler* exoplanets) to provide improved sensitivity over the Box Least Squares (BLS) method (Kovács et al. 2002).

The TLS period search on the normalised light curve of DMPP-1 yields SDE (signal detection efficiency, Kovács et al. 2002; Hippke & Heller 2019) as a function of period as shown in Figure 3a. The search covered $P = 0.60$ d (the Keplerian period at the Roche limit for a solar-type star, see Ofir 2014) to 10.88 d at with a frequency oversampling factor of 3 (Hippke & Heller 2019). While there are no peaks corresponding to the Staab et al. (2019) planets, there is a signal at $P = 3.2848 \pm 0.0085$ days with marginal significance, having SDE=6.66 and corresponding to a false-alarm probability (FAP) of arising from white noise only of 1.6%. A BLS search (with SDE calculated as described in Kovács et al. 2002) on the same data retrieves a maximum signal at $P = 3.2847$ d but with a lower value SDE=5.2 (Figure 4a) as expected (see Hippke & Heller 2019).

Parameters of the best-fitting transit model (implemented through *batman*) were found by maximum likelihood estimation, confirming the above period. Values and 16–84% credibility regions were found by sampling the posterior probability distribution using MCMC (implemented with *emcee*, Foreman-Mackey et al. 2013) assuming Gaussian priors on P (from the TLS result) and stellar density (using the stellar mass and radius values of Staab et al. 2019); and uniform priors for other parameters. Estimating parameter values from the medians of the posterior distributions gives a preferred solution of $P = 3.2854^{+0.0032}_{-0.0025}$ d, $R_{\text{P}} = 0.00100^{+0.0021}_{-0.0023} R_{*} = 1.38^{+0.29}_{-0.32} R_{\oplus}$ and $\delta = 87^{+25}_{-30}$ ppm, while the stellar density is $\rho_{*} = 0.61 \pm 0.03 \rho_{\odot}$ (see Table 1c for other parameters).

The folded light curve is shown both as cadences and running mean ($N = 41$) (Figure 3b) and binned (Figure 3c) along with the best-fitting transit model. The putative transit does not correspond to changes in the number of cadences per bin (Figure 3c) as might be expected from ineffective detrending near the start or end of the light curve. The seven individual transits have signal-to-noise ratios between 0.03 and 3.06 (Figure 3d).

Since this is a marginal signal, we investigated the sensitivity of the detection to the pre-processing carried out on the light curve. Firstly, we varied the level at which sigma-clipping is applied: at 5σ , 7 data points are excluded (as compared to 69 above), and the 3.2848 d signal has an enhanced SDE of 7.20 (Figure 4b). The likely cause is that the additional 62 data points raise the out-of-transit level, thus giving a greater significance to the dip. We conclude that a 3σ clipping level is a conservative but appropriate approach.

We investigated the sensitivity to the detrending method by using two other commonly-used methods: Savitzky-Golay (S-G) and a sliding window Tukey biweight estimator. S-G filters (see e.g. Gilliland et al. 2011) are specified by the order ($n_{\text{S-G}}$) of the detrending polynomial, and a window-width, specified here as duration in the absence of data gaps, $\Delta T_{\text{S-G}}$. We chose ranges: $n_{\text{S-G}} = [1, 2, 3]$ and $\Delta T_{\text{S-G}} = [0.25, 0.5, 1.0, 2.0, 3.0]$ d to span different timescales of variability, up to a significant fraction of the duration of contiguous data. 9 of the 15 combinations returned a maximum SDE at a period of 3.2848 d. These SDE values ranged from 7.13 to 4.96 with corresponding FAPs from 0.76% to $> 10\%$. Two of these S-G filters ($n = 1, \Delta T = 1$ d and $n = 3, \Delta T = 2$ d, Figure 4c, d respectively) returned

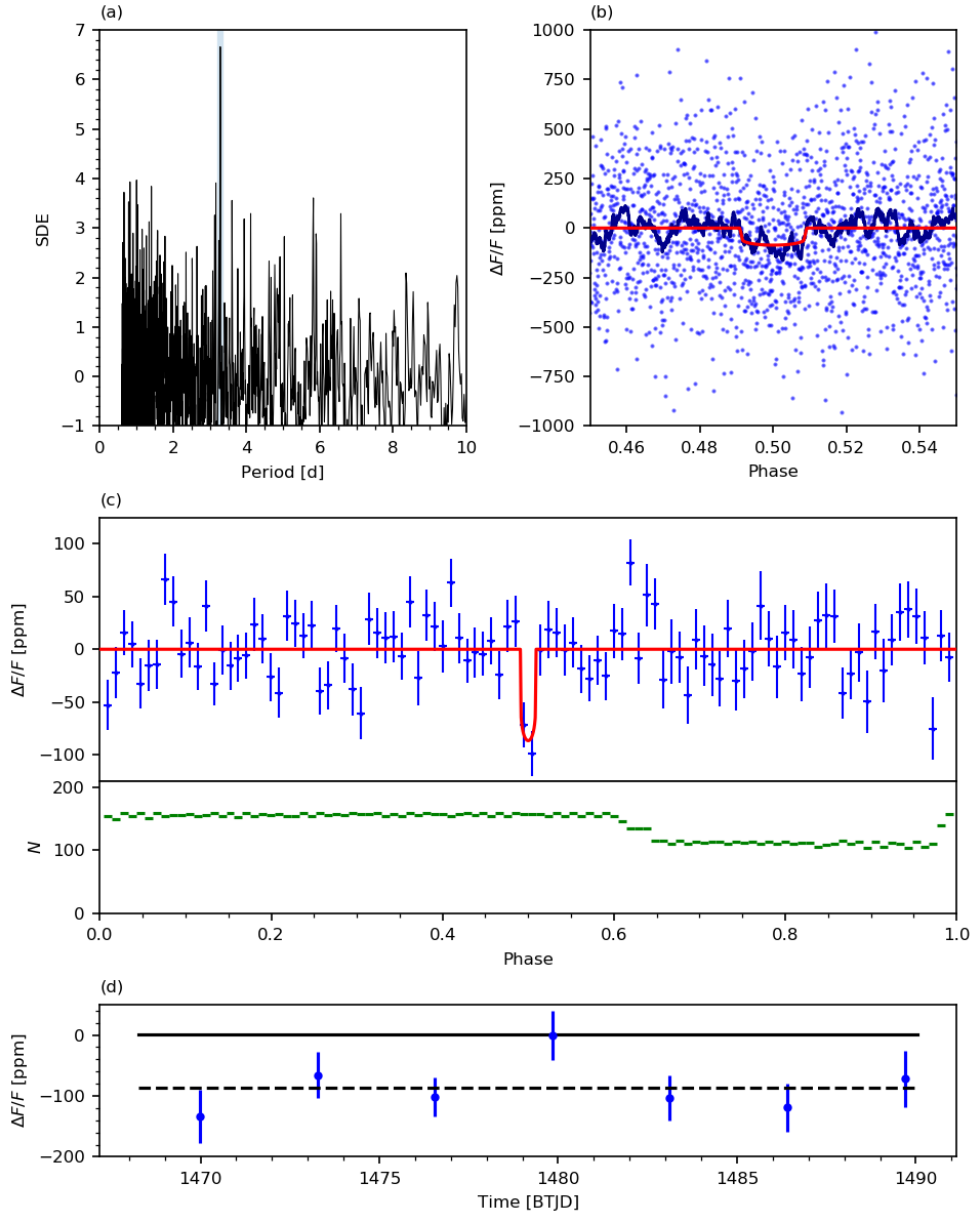


Figure 3. (a) SDE against trial period from a TLS search of the normalised TESS lightcurve of DMPP-1. (b) The lightcurve folded at the preferred solution of $P = 3.2854$ d, with a moving mean ($N = 41$ cadences) (dark blue trace) and the corresponding transit model (red). (c) The binned lightcurve folded at $P = 3.2854$ d (blue) and transit model (red). The lower panel shows the number of cadences (green) in each phase bin. (d) The individual transits of the marginal signal with the depth of the preferred solution (87 ppm) shown by the dashed line.

SDE values higher than that obtained with the GP filter. None of the light curves with $\Delta T_{S-G} = 0.25$ d recovered this signal, probably because the dip timescale is similar.

A filter based on the Tukey biweight estimator (Mosteller & Tukey 1977) was implemented through the `Wotan` package (Hippke et al. 2019). Window widths $\Delta T_{\text{biw}} = [0.25, 0.5, 1.0, 2.0, 3.0]$ d were adopted, with edge truncation of half the window width, and tuning parameter $c = 6$, appropriate for transit light curves (Hippke et al. 2019). Only $\Delta T_{\text{biw}} = 1.0$ d returned the $P = 3.2848$ d signal, and this with $SDE=4.71$ and $FAP > 10\%$.

It should be stressed that GP modelling is our preferred detrending method because the variability timescale is determined from the data (rather than arbitrary choices for ΔT_{S-G} or ΔT_{biw}). Nonetheless, the sensitivity to the

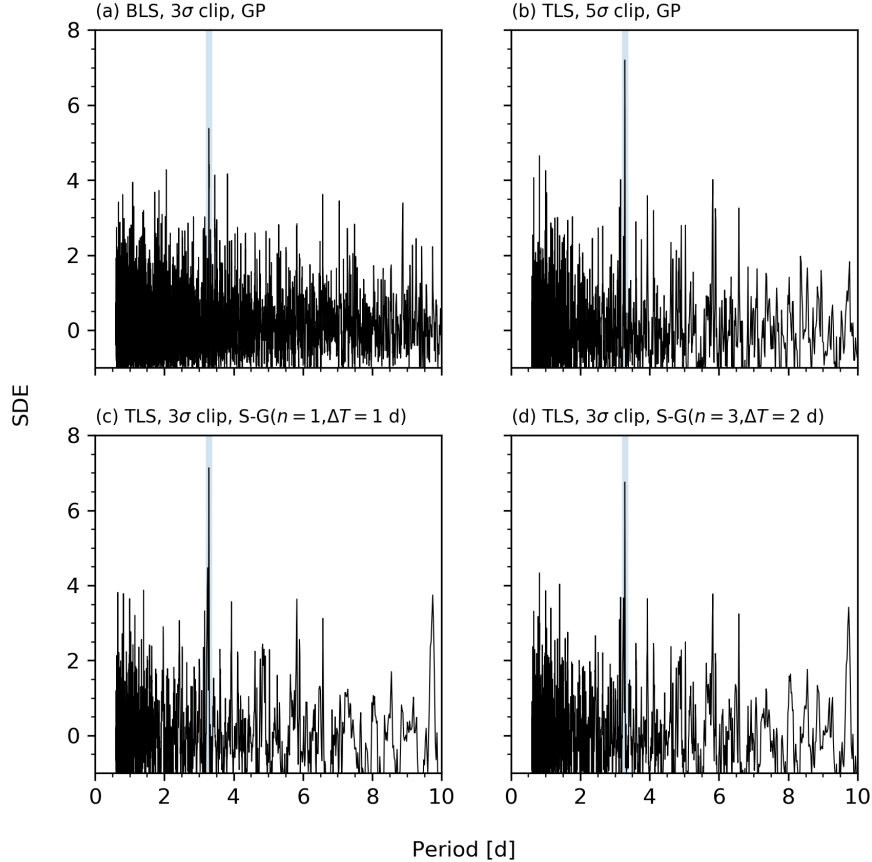


Figure 4. A comparison of BLS and TLS periodograms of the normalised TESS lightcurve of DMPP-1 using different detrending methods. (a) BLS – 3σ clip and GP detrending, (b) TLS – 5σ clip and GP detrending, (c) TLS – 3σ clip and S-G detrending ($n = 1, \Delta T = 1$ d), (d) TLS – 3σ clip and S-G detrending ($n = 3, \Delta T = 2$ d)

detrending methods implies the 3.2854 d signal is a marginal detection. Further data are needed to confirm transits at this period.

3.4. Limits and significance of modulation

The period folding method of Section 3.1 was used to find transit detection limits on the same period grid as our TLS search. Noting that such limits are a compromise between sensitivity and measurement timescale, we adopted a bin-width of $0.4T_{\text{dur, max}}$ (i.e. sensitive to transits with $b < 0.917$) since this is expected to show the modulation due to the 3.2854 d signal and allow its significance to be estimated independently of the SDE value returned by TLS. In general, at a given folding period, the value of σ_{bin} varies with phase (c.f. Fig. 3c). Consequently we show two quantities in Figure 5: $A_{5\sigma, \text{max}}$ (thick cyan line) and $A_{5\sigma, \text{mean}}$ (thin cyan line) defined as 5 times the maximum and mean values of σ_{bin} respectively. In the absence of a detected signal, $A_{5\sigma, \text{max}}$ provides the firm upper limit to any modulation that may be present, and at short periods ($P < 3$ days) it is well-represented by

$$A_{5\sigma, \text{max}} = 64(P/\text{days})^{0.36} \text{ppm} \quad (1)$$

(dashed line in Figure 5). At longer periods $A_{5\sigma, \text{max}}$ exhibits step-like behaviour with increasing P , arising from large changes in the minimum number of cadences per phase bin. $A_{5\sigma, \text{mean}}$ indicates the typically detectable depth threshold.

Figure 5 also shows the maximum detected modulation (red dots) of all transit-like (i.e. dip) signals. Also shown (red circle) is the result of folding at 3.2854 d: this yields $\Delta F/F = 94$ ppm and $5.4\sigma_{\text{bin}}$ significance ($1.01 \times A_{5\sigma, \text{mean}}$).

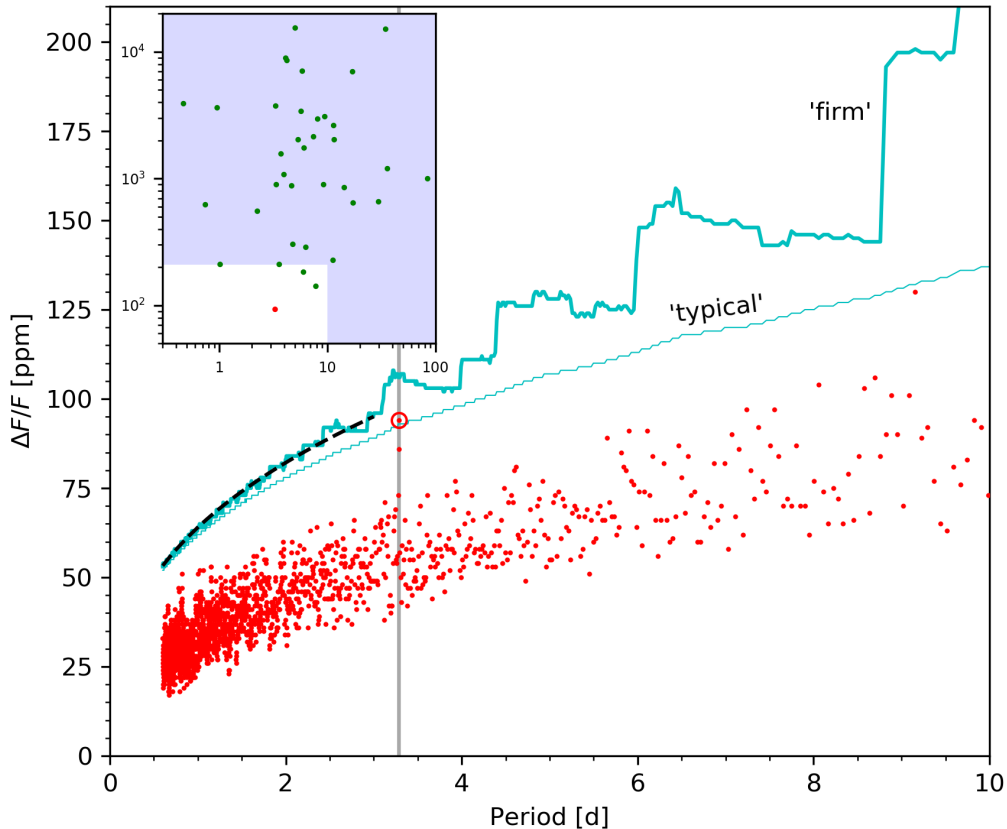


Figure 5. Measurements and limits of the amplitude of modulation in the TESS light curve of DMPP-1. Actual modulations (red dots) are the maximum dip-like changes in a single phase bin (corresponding to $0.4T_{\text{dur, max}}$) at a given period. The thick cyan line shows the firm upper limit to modulation ($A_{5\sigma, \text{max}}$) while the thin cyan line shows the typical level of modulation ($A_{5\sigma, \text{mean}}$) that is potentially detectable. The dashed black line at $P < 3$ d shows an approximate analytical form to the firm amplitude limit. The red circle shows the modulation at $P = 3.2854$ d. (Note that the modulation at 9.16 d that is near the ‘typical’ detection curve has a significance of $3.3\sigma_{\text{bin}}$) The inset shows the context of the $P = 3.2854$ d signal (red dot) in relation to all TESS exoplanets (green dots) with amplitudes calculated as $(R_P/R_*)^2$.

The FAP for a $5\sigma_{\text{bin}}$ variation in this search for DMPP-1 is calculated by noting that there are 70217 independent combinations of period and phase bin (the number of independent periods was found using Equation 6 of Ofir 2014). Multiplying this by the one-sided probability of a 5σ deviation (2.87×10^{-7}) gives $\text{FAP} = 2.0\%$. Since the signal exceeds $5\sigma_{\text{bin}}$, $\text{FAP} < 2.0\%$ and is consistent with the value found by TLS.

4. DISCUSSION

4.1. No transits of RV planets

The TESS photometry does not reveal any transits corresponding to the planets reported by Staab et al. (2019). If these planets are of Earth-like rocky composition, or have compositions similar to Solar System ice giants, their radii imply transit depths for edge-on orbits which exceed our detection thresholds. We conclude that either the planets are not in orbits that transit the host star, or that no transit of (Neptune-like) planets happened to occur during the TESS observation, or that (super-Earth) planets are smaller than models based on Solar System planets (Zeng et al. 2019) would predict.

The extent of the circumstellar gas cloud can be estimated assuming that the lack of observed transits is due to orbital inclination. As noted by [Staab et al. \(2019\)](#), the cloud could originate from any of the super-Earth planets (-1c, d, e, or d', e', f'). Adopting a simple geometric model in which the gas cloud extends a height h vertically from the orbital plane, then the requirement that the cloud completely covers the stellar photosphere but that the planet does not transit implies $h \geq 2R_*/[1 - (R_*/a)^2]^{1/2}$. Assuming azimuthal symmetry, the solid angle subtended by the cloud from the centre of the star is $\Omega_c \geq 4\pi(2/[3 + (a/R_*)^2]^{1/2})$. The fraction of the sky covered by the cloud $> 27\%$ if it originates from DMPP-1 d with $P \approx 3$ d ($> 16\%$ for DMPP-1 c with $P \approx 6.5$ d).

4.2. Insolation of DMPP-1 planets and known CDEs

Supplementary Figure 4b of [Staab et al. \(2019\)](#) establishes that the DMPP-1 planets are among the most irradiated known low mass planets orbiting bright, nearby stars. They fall along the lower boundary of the Neptune desert. The insolation values, S , of DMPP-1 b, c, d and e are tabulated in Table 1. DMPP-1 d's insolation is similar to that of Kepler-1520 b ($1134_{-54}^{+57} S_\oplus$, [Berger et al. 2018](#)). The other two known CDEs: K2-22b ([Sanchis-Ojeda et al. 2015](#)) and KOI-2700b ([Rappaport et al. 2014](#)) are less irradiated with insolation fluxes of $738_{-197}^{+243} S_\oplus$ ([Dressing et al. 2017](#)) and $801_{-31}^{+32} S_\oplus$ ([Berger et al. 2018](#)) respectively. Coupled with the circumstellar gas which apparently surrounds DMPP-1, this constitutes grounds to suspect that the planets orbiting DMPP-1 may have been significantly eroded as a consequence of proximity to their luminous F8V host star. The DMPP-1 planets are probably not pure iron, but they may not be very much bigger than this limiting model. Table 1 and Figure 5 show that planets DMPP-1 d, e, e' and f' are either undetectable or close to the detection threshold. We need to drive down the detection thresholds with more precise photometry, e.g. with CHEOPS observations.

4.3. Marginal Detection of a $P=3.2854$ day CDE?

We marginally detect a transit signal with $P = 3.2854$ d in the TESS data. If this were due to an Earth-like rocky planet, it would correspond to a planet of mass $3.2_{-2.0}^{+3.6} M_\oplus$. The RV data of [Staab et al. \(2019\)](#) shows no evidence for modulation at this period.

We carried out orbital integrations, using IAS15 within REBOUND ([Rein & Spiegel 2015; Rein & Liu 2012](#)), for the DMPP-1 system of 4 planets, adding the putative 3.2854 d Planet 5. Assuming circular orbits ($e = 0$), and adopting a range of masses for Planet 5, we find that all configurations remain stable for 10^5 yrs for masses $\leq 3.5 M_\oplus$.

Since [Staab et al. \(2019\)](#) found upper limits to the eccentricities of $e = 0.083, 0.057, 0.07, 0.07$ for DMPP-1 b, c, d, e, we also carried out eccentric orbital integrations at these limits including Planet 5 (with $e = 0.07$). As expected, the system is unstable for all masses of Planet 5 since it crosses the orbit of DMPP-1 d. Considering the 0.006 AU Hill sphere of DMPP-1 d and assuming a negligible mass for Planet 5 indicates an upper eccentricity limit of $e = 0.04$ for both planets. The true value will be smaller owing to the influence of DMPP-1 b, c and e. Hence if the 3.2854 d planet exists, the orbits of all DMPP-1 planets must be very close to circular, with somewhat lower eccentricities than the upper limits reported by [Staab et al. \(2019\)](#).

A planet in a circular orbit around DMPP-1 with $P=3.2854$ d would suffer an insolation of $990 S_\oplus$, typical for a CDE. The marginal evidence for variable transit depth in Fig. 3d could indicate that the transits are akin to those of Kepler-1520 b. If this were the case, we would expect a tiny reflex RV modulation.

In the case of Kepler-1520 b, transits are due to a dust cloud ([Rappaport et al. 2012; Brogi et al. 2012; Bochinski et al. 2015](#)) rather than the planet itself. If the $P = 3.2854$ d signal arises in an analogous way, then assuming grain radius s , dust density ρ , and dust sublimation rate τ_{dust} , we estimate the dust mass as

$$M_{\text{dust}} \approx 9 \times 10^{14} \left(\frac{\rho}{3 \text{ g cm}^{-3}} \right) \left(\frac{s}{1 \mu\text{m}} \right) \text{ g}, \quad (2)$$

and the rate of dust production as

$$\dot{M}_{\text{dust}} \sim 3 \times 10^{10} \left(\frac{\rho}{3 \text{ g cm}^{-3}} \right) \left(\frac{s}{1 \mu\text{m}} \right) \left(\frac{\tau_{\text{dust}}}{3 \times 10^4 \text{ s}} \right)^{-1} \text{ g s}^{-1}, \quad (3)$$

about one third of Kepler-1520 b's value, $\dot{M}_{\text{dust}} \sim 10^{11} \text{ g s}^{-1}$ ([Rappaport et al. 2012](#)).

4.4. Metal-rich gas from ablating planets

Metal-rich gas must co-exist with the dusty effluents from CDEs (Rappaport et al. 2012; Ridden-Harper et al. 2019). A search for traces of this circumstellar gas in the Na D and Ca II infrared triplet lines in spectra of K2-22 yielded null results and a range of upper limits (Ridden-Harper et al. 2019). DMPP-1 is already known to exhibit circumstellar absorption (Staab et al. 2019; Haswell et al. 2019), so if the marginal transit detection reported herein does prove to be a CDE, this system will be the best yet known to trace the gas loss and sublimation processes discussed in Ridden-Harper et al. (2019). DMPP-1 is almost 8 magnitudes brighter than K2-22 in the V band. Thus this system offers exciting scope for high temporal and spectral resolution studies.

4.5. Hot rocky planet compositions

The atmospheric compositions of hot rocky planets have been modelled by Schaefer & Fegley (2009); Miguel et al. (2011); Schaefer et al. (2012); Lupu et al. (2014); Ito et al. (2015). The atmospheric absorption in the UV and IR is dominated by SiO, and the short wavelength absorption causes a temperature inversion, promoting the formation of strong spectral features. Kite et al. (2016) model the processes governing the gas and dust escape from a hot rocky planet. They find two cases: magma-ocean-dominated and silicate-atmosphere dominated. In the latter case, which applies to the hottest planets with equilibrium temperature, $T_{\text{eq}} > 2400$ K, wind transport dominates and the magma pools are compositionally patchy. The chemical abundance mix in the mass loss can consequently be variable. The outflow from the putative CDE causing our marginally detected transit signal could potentially allow us to directly probe this compositional variability.

Surface compositional heterogeneity is not fully understood even for the Earth (Rizo et al. 2016), and may provide traces of the primary accretion phase of planet formation. The potential to observe the surface composition variations of exoplanets offers a valuable counterpoint to the Solar System based picture of planetary system formation.

5. SUMMARY AND CONCLUSIONS

1. DMPP-1 is a bright, nearby star, hosting a compact multi-planet system. We expect the DMPP-1 planetary orbits to be aligned approximately edge-on as ablated planetary gas fills our line of sight to the chromospherically active regions of the star.
2. We analysed the TESS data for DMPP-1, performing a sensitive search for transits of the RV planets reported by Staab et al. (2019). We find null results, suggesting that perhaps these planets are denser than conventional Earth-like rocky planets. Alternatively, the DMPP-1 RV planets are not exactly edge-on.
3. We marginally detect (with FAP of 1.6%) a 87_{-30}^{+25} ppm transit with a period of $P = 3.2854_{-0.0025}^{+0.0032}$ d. One of the 7 transits has a depth consistent with zero, reminiscent of the variable transit depths of the known CDEs.
4. The $P = 3.2854_{-0.0025}^{+0.0032}$ d period corresponds to insolation $S = 990S_{\oplus}$, typical of CDEs. A CDE would be well below the RV detection threshold.
5. The detection of the $P = 3.2854_{-0.0025}^{+0.0032}$ d signal is sensitive to the detrending approach adopted. We therefore consider our detection marginal. Small planets orbiting solar type stars are challenging to find in a single sector of TESS data. Further sectors of TESS data and targeted photometry with CHEOPS will be helpful in the assessment of marginal signals.
6. JWST will be very sensitive to SiO gas which is expected in material ablated from hot rocky planets including CDEs. DMPP-1 could be an excellent candidate for IR spectroscopy with JWST to examine hot rocky planet compositions.

ACKNOWLEDGEMENTS

CAH and JRB are supported by STFC Grants ST/P000584/1 and ST/T000295/1. DS was supported by an STFC studentship.

REFERENCES

- Berger, T.A., Huber, D., Gaidos, E., van Saders, J.L. 2018, ApJ, 866, 99
- Bochinski, J. J., Haswell, C. A., Marsh, T. R., et al. 2015, ApJL, 800, L21

- Bodman, E.H.L., Wright, J.T., Desch, S.J., Lisse, C.M. 2018, *AJ*, 156, 173
- Brogi, M., Keller, C. U., de Juan Ovelar, M., et al. 2012, *A&A*, 545, L5
- Dressing, C.D., Vanderburg, A., Schlieder, J.E. et al. 2017, *ApJ*, 154, 207
- Foreman-Mackey, D., Agol, E., Ambikasaran, S., et al. 2017, *AJ*, 154, 220
- Foreman-Mackey, D., Hogg, D. W., Lang, D., et al. 2013, *PASP*, 125, 306
- Fossati, L., Ayres, T. R., Haswell, C. A., et al. 2013, *ApJL*, 766, L20
- Gilliland, R. L., Chaplin, W. J., Dunham, E. W., et al. 2011, *ApJS*, 197, 6
- Haswell, C. A., Fossati, L., Ayres, T., France, K., Froning, C.S. et al. 2012, *ApJ*, 760, 79
- Haswell, C. A., Staab, D., Barnes, J. R., et al. 2019, *Nature Astronomy*, 2
- Heller, R. 2019, *A&A*, 623, A137
- Hippke, M., David, T. J., Mulders, G. D., et al. 2019, *AJ*, 158, 143
- Hippke, M., & Heller, R. 2019, *A&A*, 623, A39
- Ito, Y., Ikoma, M., Kawahara, H., Nagahara, H., Kawashima, Y., Nakamoto, T. 2016, *ApJ*, 801, 144
- Kite, E.S., Fegley, B., Schaefer, L., Gaidos, E. 2016, *ApJ*, 828, 80
- Kovács, G., Zucker, S., & Mazeh, T. 2002, *A&A*, 391, 369
- Kreidberg, L. 2015, *PASP*, 127, 1161
- Léger, A., Rouan, D., Schneider, J., et al. 2009, *A&A*, 506, 287
- Lightkurve Collaboration, Cardoso, J. V. de M., Hedges, C., et al. 2018, Lightkurve: Kepler and TESS time series analysis in Python, ascl:1812.013
- Lupu, R.E., Zahnle, K., Marley, M.S. et al. *ApJ*, 784, 27
- Miguel, Y., Kaltenegger, L., Fegley, B., Schaefer, L. 2011, *ApJL*, 742, L19
- Mosteller, F., & Tukey, J. W. 1977, Addison-Wesley Series in Behavioral Science: Quantitative Methods
- Noyes, R. W., Hartmann, L. W., Baliunas, S. L., et al. 1984, *ApJ*, 279, 763
- Ofir, A. 2014, *A&A*, 561, A138
- Price, E.M., Rogers, L.A. 2019, *ApJ* submitted; arXiv:1901.10666
- Rappaport, S., Levine, A., Chiang, E., et al. 2012, *ApJ*, 752, 1
- Rappaport, S., Barclay, T., DeVore, J., et al. 2014, *ApJ*, 784, 40
- Rein, H., & Liu, S.-F. 2012, *A&A*, 537, A128
- Rein, H., & Spiegel, D. S. 2015, *MNRAS*, 446, 1424
- Ricker, G. R., Winn, J. N., Vanderspek, R., et al. 2015, *Journal of Astronomical Telescopes, Instruments, and Systems*, 1, 014003
- Ridden-Harper, A.R., Snellen, I.A.G., Keller, C.U., and Mollière, P. 2019, *A&A*, 628, A70
- Rizo, H., Walker, R.J., Carlson, R.W., Horan, M.F., Mukhopadhyay, S. et al. 2016, *Science*, 352, 809
- Sanchis-Ojeda, R., Rappaport, S., Pallé, E. et al. 2015, *ApJ*, 812, 112
- Schaefer, L., Lodders, K., Fegley, B. 2012, *ApJ*, 755, 41
- Schaefer, L., Fegley, B. 2009, *ApJL*, 703, L113
- Smith, J. C., Stumpe, M. C., Jenkins, J. M., et al. 2017, Kepler Science Document
- Staab, D., Haswell, C. A., Barnes, J. R., et al. 2019, arXiv e-prints, arXiv:1912.10792
- Staab, D., Haswell, C. A., Smith, G. D., et al. 2017, *MNRAS*, 466, 738
- Stassun, K. G., Oelkers, R. J., Pepper, J., et al. 2018, *AJ*, 156, 102
- Tenenbaum, P., & Jenkins, J. 2018, NASA Technical report, NASA/TM2018220036
<https://archive.stsci.edu/missions/tess/doc/EXP-TESS-ARC-ICD-TM-0014.pdf>
- Zeng, Li, Jacobsen, Stein B., Sasselov, D.D., et al. 2019, *PNAS*, 116, 9723-9728. DOI: 10.1073/pnas.181295116